J Appl Physiol 115: 1822–1837, 2013.
First published September 26, 2013; doi:10.1152/japplphysiol.00589.2013.

A 3-D mathematical model to identify organ-specific risks in rats during thermal stress

Vineet Rakesh,[1] Jonathan D. Stallings,[2] Bryan G. Helwig,[3] Lisa R. Leon,[3] David A. Jackson,[2] and Jaques Reifman[1]

[1]*Department of Defense Biotechnology High Performance Computing Software Applications Institute, Telemedicine and Advanced Technology Research Center, United States Army Medical Research and Materiel Command, Fort Detrick, Maryland;* [2]*Biomarkers Program, United States Army Center for Environmental Health Research, Fort Detrick, Maryland; and* [3]*Thermal Mountain Medicine Division, United States Army Research Institute of Environmental Medicine, Natick, Massachusetts*

Submitted 15 May 2013; accepted in final form 24 September 2013

Rakesh V, Stallings JD, Helwig BG, Leon LR, Jackson DA, Reifman J. A 3-D mathematical model to identify organ-specific risks in rats during thermal stress. *J Appl Physiol* 115: 1822–1837, 2013. First published September 26, 2013; doi:10.1152/japplphysiol.00589.2013.—Early prediction of the adverse outcomes associated with heat stress is critical for effective management and mitigation of injury, which may sometimes lead to extreme undesirable clinical conditions, such as multiorgan dysfunction syndrome and death. Here, we developed a computational model to predict the spatiotemporal temperature distribution in a rat exposed to heat stress in an attempt to understand the correlation between heat load and differential organ dysfunction. The model includes a three-dimensional representation of the rat anatomy obtained from medical imaging and incorporates the key mechanisms of heat transfer during thermoregulation. We formulated a novel approach to estimate blood temperature by accounting for blood mixing from the different organs and to estimate the effects of the circadian rhythm in body temperature by considering day-night variations in metabolic heat generation and blood perfusion. We validated the model using in vivo core temperature measurements in control and heat-stressed rats and other published experimental data. The model predictions were within 1 SD of the measured data. The liver demonstrated the greatest susceptibility to heat stress, with the maximum temperature reaching 2°C higher than the measured core temperature and 95% of its volume exceeding the targeted experimental core temperature. Other organs also attained temperatures greater than the core temperature, illustrating the need to monitor multiple organs during heat stress. The model facilitates the identification of organ-specific risks during heat stress and has the potential to aid in the development of improved clinical strategies for thermal-injury prevention and management.

computational modeling; core temperature; finite element method; multiorgan dysfunction syndrome; radiotelemetry

HEAT STRESS is characterized by an increase in body temperatures from exposure to hot weather conditions (6). Severe heat stress leads to heat stroke, which may trigger a complex cascade of events emanating from thermoregulatory failure to systemic inflammatory response and eventually to multiple organ dysfunction syndrome (MODS) (6, 24, 55). It is a life-threatening condition and may also lead to increased risk of mortality in the long term (3, 79). Military personnel (4) as well as athletes (11) undergoing strenuous physical activity in hot and humid environments are at great risk for exertional heat stress, which may occur in healthy young adults (61, 89). For example, in the United States military, 14,577 cases of heat-related injuries were reported between 2007 and 2011, which resulted not only in significant lost-duty days and associated medical costs but also in life-threatening conditions (4, 10). One potential strategy to reduce the high incidence of heat-stress cases and minimize injury progression is to establish the ability to accurately predict impending rises in organ temperatures (37, 38). In fact, the need for the early prediction of impending temperature rises and the adverse effects associated with heat stress has been recognized as an integral part of effective injury management and mitigation strategies (6, 39, 55).

Injury progression from the initial thermal insult to MODS and potential mortality is a complicated process, and in vivo animal studies have been frequently used to elucidate the associated pathogenesis and pathophysiology (7, 16, 54, 88). In such studies, heat stress is generally induced by placing the animal in a temperature-controlled chamber where its core temperature is remotely monitored using telemetry probes surgically implanted into the abdominal cavity or via measurements of rectal or skin temperature using thermocouples (7, 16, 54, 88). However, in vivo monitoring in these studies is limited to transient temperature measurements at a single location in the animal, failing to provide information about the temperature distribution and presence of "hot spots" in the various organs. The evaluation of temperature distribution and identification of hot spots are important as the order and severity of organ dysfunction in MODS is dependent on the inflammatory response, which in turn depends, at least partially, on the thermal injury (6, 24, 80). Because differences in anatomy and heat transfer properties can lead to distinct thermal injury in different organs, invoking differential tissue damage and organ dysfunction (42, 53, 80), it is critical to spatially monitor the temperature in various organs to obtain greater insights on disease progression. In the absence of experimental methods, a computational model based on a realistic description of an animal's anatomy and capable of emulating the underlying thermoregulatory mechanisms would be useful for quantifying the spatial distribution and temporal dynamics of temperatures in the entire body. Such a model would facilitate the prediction of the time and extent of organ damage as a function of thermal stress.

Even under normothermic conditions, visceral organs have different temperatures, which depend on the heat produced by cell metabolism and heat exchange due to blood perfusion in

Address for reprint requests and other correspondence: J. Reifman, DoD Biotechnology High Performance Computing Software Applications Institute, Telemedicine and Advanced Technology Research Center, U.S. Army Medical Research and Materiel Command, MCMR-TT, 504 Scott St., Fort Detrick, MD 21702-5012 (e-mail: jaques.reifman.civ@mail.mil).

the particular organ (15). Figure 1 shows the various mechanisms of heat transfer inside the body. Conduction and convection due to blood perfusion facilitate heat transfer between the various organs. Heat is lost by convection, radiation, and evaporation of sweat or saliva (in animals that do not have sweat glands) from the skin surface at normothermia. Consequently, owing to these heat-loss mechanisms, the skin is typically at a lower temperature compared with the core (15, 33). During heat stress, external environmental conditions and/or exertion lead to an increase in body temperature, triggering a complex physiological response that aims to restore normothermia (24). An increase in body temperature during heat stress induces an increase in cardiac output, skin blood perfusion, and perspiration/salivation to facilitate heat loss (6). The blood vessels in the visceral organs vasoconstrict, whereas the skin blood vessels vasodilate to accommodate blood redistributed from the core to the body surface by the cardiovascular system (6). The increases in skin blood flow and evaporation rate due to perspiration/salivation enhance the rate of heat loss in the body, as it attempts to cool down. Body temperature rises when the rate of heat loss is unable to match the heat gained due to thermal stress while also accounting for metabolic heat generation and heat transfer away from the organ. To accurately quantify the temperature distribution in the body both during normothermic and thermal-stress conditions, key thermoregulatory mechanisms need to be incorporated into the computational model.

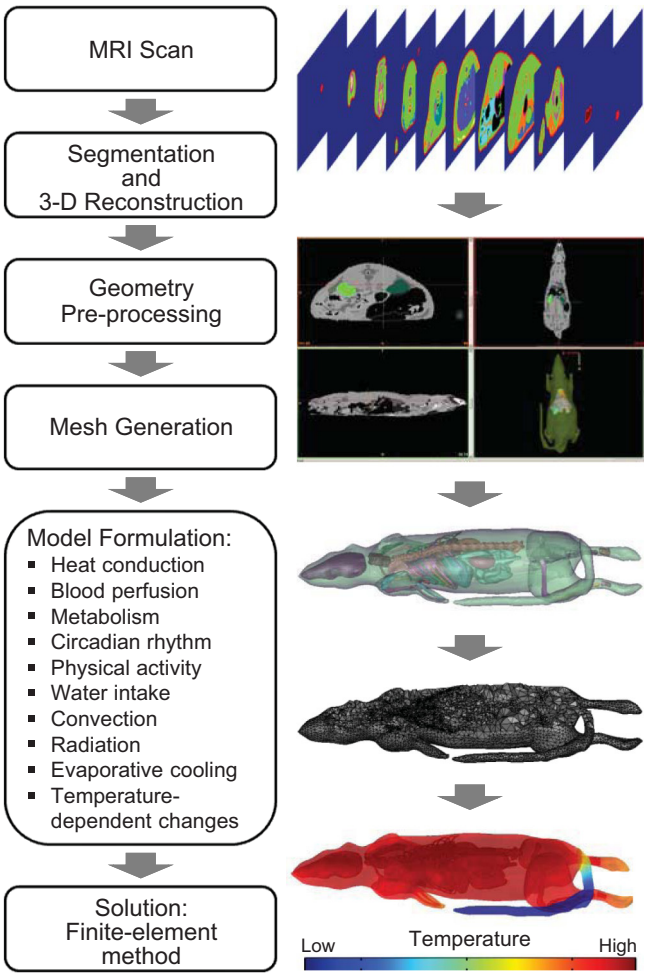

Fig. 1. Steps in the development of the computational model. The preliminary anatomical model was acquired from Duke University. The anatomical features that were missing from the preliminary model were reconstructed from stacks of magnetic resonance images obtained from Brooks Air Force Base. Preprocessing of the geometry for subsequent computations using finite-element method was performed in Mimics and 3-matic (Materialise, Plymouth, MI). The mathematical model was formulated by incorporating the heat-transfer mechanisms shown and was solved in COMSOL Multiphysics (COMSOL, Burlington, MA). MRI, magnetic resonance imaging; 3-D, three-dimensional.

Numerous studies have focused on the development of whole body computational models of thermoregulation for animal models and humans (5, 27, 32, 35, 40, 44, 46, 71, 72). However, most of these studies have grossly simplified the anatomy by, for example, considering a one-dimensional radial representation or assuming regular shapes, such as cylinders and spheres, for organs and body contours (27, 35, 40, 65). While some included anatomically realistic description of the geometry, the emphasis of most of these models was on the short-term evaluation of temperature distribution to gauge the effects of electromagnetic irradiation (5, 44, 71, 75, 76). Consequently, owing to the short time scales (30–5,400 s) of these studies, the models did not attempt to describe longer periodic phenomena (>24 h), such as circadian variations, or used simplifying assumptions, such as constant blood temperature, during the heating process. Furthermore, some models even ignored critical heat transfer mechanisms, such as convection due to blood perfusion (71). Heat transfer models for other applications, such as burn injury and thermal therapy, have focused on only the organ or region of interest without including the whole body anatomy (22, 23, 57, 90). However, due to heat transfer by cardiovascular blood flow and other mechanisms, such as thermal conduction, thermal responses in the various organs are interdependent. Moreover, as discussed above, severe heat stress may lead to a systemic inflammatory response and varying severity of dysfunctions in different organs. Therefore, to investigate the progression of heat stress and elucidate the differential response in different organs, it is imperative that the computational model characterizes the whole body thermal response during and after the heat-stress period.

In this work, we present a computational approach to predict the temporal dynamics and spatial temperature distribution for an in vivo rat model. Our computational model includes three-dimensional (3-D) geometry obtained from medical imaging to accurately characterize the rat anatomy. Our mechanistic computational modeling approach incorporates various mechanisms of heat transfer associated with thermal stress, including heat conduction, blood perfusion, metabolic heat generation, physical activity, water intake, evaporative cooling, and external convection and radiation. The model includes novel formulations for computing blood temperature as well as the circadian rhythm in body temperature, which have not been considered in previous efforts. We validated the predicted core temperature and its circadian variation, organ volumes, and organ temperatures using in vivo animal experiments and literature data. The model provides the capability to predict the temperature distribution within each vital organ and potentially establish correlations with impending inflammatory responses and differential organ dysfunction. This, in turn, will facilitate the identification of organ-specific risks due to exposure to

thermal stress, such as acute liver failure and brain inflammation (13, 31). In addition, it would potentially aid in the development of improved clinical strategies for prevention and management of heat stress, such as design of localized cooling strategies (47).

Glossary

A	Surface area (m^2)
AL	Activity level (dimensionless)
ac	Relative activity level (dimensionless)
ac_{max}	Maximum relative activity level (dimensionless)
a_{met}	Amplitude of circadian variation in metabolic heat generation (dimensionless)
a_{per}	Amplitude of circadian variation in blood perfusion (dimensionless)
c_p	Specific heat capacity ($J \cdot kg^{-1} \cdot °C^{-1}$)
$c_{p,b}$	Specific heat capacity of blood ($J \cdot kg^{-1} \cdot °C^{-1}$)
$c_{p,water}$	Specific heat capacity of water ($J \cdot kg^{-1} \cdot °C^{-1}$)
C_{met}	Circadian function for metabolic heat generation (dimensionless)
C_{per}	Circadian function for blood perfusion (dimensionless)
d	Characteristic diameter (m)
h_c	Convective heat transfer coefficient ($W \cdot m^{-2} \cdot °C^{-1}$)
k	Thermal conductivity ($W \cdot m^{-1} \cdot °C^{-1}$)
L_{water}	Latent heat of vaporization of water (J/kg)
M	Body mass (kg)
m_{water}	Experimentally measured water intake (kg)
$\dot{m}_{saliva}$	Rate of saliva loss (kg/s)
n	Direction normal to the skin surface (dimensionless)
Q_m	Metabolic heat generation rate (W/m^3)
Q_{m0}	Basal metabolic heat generation rate (W/m^3)
Q_{loss}	Volumetric heat loss due to water intake (W/m^3)
T	Body temperature at a given *x, y, z* location (°C)
t	Time (s)
T_0	Reference temperature at steady state (°C)
T_a	Arterial blood temperature (°C)
T_{amb}	Ambient temperature (°C)
T_c	Core temperature (°C)
T_L	Body-temperature limit corresponding to baseline blood perfusion (°C)
T_{skin}	Skin surface temperature (°C)
T_U	Body-temperature limit corresponding to elevated or depressed blood perfusion (°C)
T_{water}	Water temperature (°C)
u	Air flow velocity (m/s)
V	Organ volume (m^3)
$\dot{V}_{b0}^v$	Basal blood perfusion rate ($m^3 \cdot s^{-1} \cdot m^{-3}$)
$\dot{V}_b^v$	Blood perfusion rate ($m^3 \cdot s^{-1} \cdot m^{-3}$)
$\dot{V}_{b,HS}^v$	Blood perfusion rate under heat-stress conditions ($m^3 \cdot s^{-1} \cdot m^{-3}$)
$V_{stomach}$	Volume of stomach (m^3)
α	Coefficient for linear increase in perfusion with temperature (dimensionless)
β	Coefficient for linear decrease in perfusion with temperature (dimensionless)
Δt	Time step size (s)
Δt_{water}	Water intake time interval (s)
ε	Emissivity (dimensionless)
η	Mechanical efficiency in metabolic heat generation
μ	Dynamic viscosity (Pa·s)
ρ	Density (kg/m^3)
ρ_b	Density of blood (kg/m^3)
σ	Stefan–Boltzmann constant (5.67×10^{-8} $W \cdot m^{-2} \cdot °C^{-4}$)
τ	Period of the circadian oscillator (s)
φ_{met}	Circadian phase for metabolic heat generation (dimensionless)
φ_{per}	Circadian phase for blood perfusion (dimensionless)

MATERIALS AND METHODS

The computational model was formulated by including a 3-D representation of the rat geometry obtained from magnetic resonance imaging (MRI) and describing the dominant modes of heat transfer during thermoregulation. Simulations were performed for control and heat-stress conditions that mimicked the experimental conditions. The details of model development steps are illustrated in Fig. 1 and discussed below along with the experimental protocol.

Experimental Protocol

Simulations were set up based on in vivo rat experiments performed at the U.S. Army Research Institute of Environmental Medicine (USARIEM). The Institutional Animal Care and Use Committee approved all experimental procedures, which were performed in accordance with the American Physiological Society's Guiding Principles for Research Involving Animals and adhered to the National Institutes of Health *Guide for Care and Use of Laboratory Animals*.

Animals. A power analysis, performed using core temperature data from a previous rat heat-stress study, indicated that $n = 15$ control rats and $n = 15$ heat-stressed rats were needed to achieve statistical significance for observing mean differences of 0.5°C between the two groups during recovery after heat stress. However, in this study, we leveraged data for model development and validation from a larger study ($n = 80$) designed to establish a plasma and tissue bank for control ($n = 30$) and surviving (>1 day) heat-stressed ($n = 50$) animals. Male Fischer 344 (F344; $n = 80$; Charles River Laboratories, Stone Ridge, NY) rats weighing 234–336 g (~2–3 mo old) were used. Animals were obtained in five separate shipments, with rats randomly assigned to heat-stressed and control groups. Rats were individually housed in Nalgene polycarbonate cages (10.5 × 19 × 8 in., Ancare, Bellmore, NY) with HEPA-filter cage tops and ALPHA-dri/Cob blend bedding (PharmServ, Framingham, MA). Environmental enrichment consisted of a rat Igloo (Nalgene Nunc, Rochester, NY), a small plastic ball, a Nylabone for chewing, and a Maplewood product containing a food treat to encourage foraging (W0002, Bio-Serv, Frenchtown, NJ). Rats were housed under standard laboratory conditions (22.0 ± 0.2°C, 12:12-h light-dark cycle, lights on at 0600) in an Association for Assessment and Accreditation of Laboratory Animal Care-accredited facility. A relatively cool housing temperature (22.0 ± 0.2°C) was chosen for these experiments to ensure rapid cooling and survival during heat-stress recovery. Rodent laboratory chow (LM-485, Harlan Teklad, Madison, WI) and water were provided ad libitum except during experimental procedures. Water ingested by the animals was measured.

Radiotelemetry measurements. Rats were implanted with TL11M2-C50-PXT PhysioTel Multiplus Transmitters (Data Sciences, St. Paul, MN) 10 days before arrival at USARIEM. The temperature sensors were implanted in the intraperitoneal cavity and were sutured to the peritoneal wall. The transmitters measured core temperature (T_c; ±0.25°C) and did not produce thermal energy on implantation. Each transmitter emitted a unique frequency that was proportional to T_c and was received by an antenna under the cage of each animal. All radiotelemetry variables were monitored at 1-min intervals in con-

scious, free-ranging animals that maintained normal heat dissipation mechanisms. Implanted transmitters weighed ~11 g or ~3–4% of the experimental body weight of the animal. Animals were housed for ≥1 wk before experimental protocols to acclimatize to the environmental conditions and ensure a robust circadian T_c rhythm before experimentation. We calculated the average daytime T_c values (0600–1759) for all rats for 2 days prior to experimentation (after the acclimatization period to our facility) and used this value (37.3°C) as the criterion for baseline temperature at which heat stress could be initiated for each animal.

Heating protocol. All experiments were conducted in conscious, free-moving animals. Randomly assigned rats, in their original cage with filter tops removed, were placed in a floor standing incubator (Thermo Scientific, Ashville, NC) set at room temperature (22.0 ± 0.2°C) 24 h before the initiation of heat-stress experiments. Non-heated rats were not introduced to the incubator environment and remained in their original cage and rack location throughout the heating protocols. Heat-stress experimentation was initiated between 0800 and 1000, after the T_c of each rat reached values below 37.3°C (the 12-h daytime average T_c of all animals as discussed above). The heating experiments were initiated by weighing rats in the heat-stressed ($n = 50$) and control ($n = 30$) groups followed by removal of food and water. Rats in the heat-stressed group were placed in the incubator in their original cage, and the incubator temperature was increased to 37.0 ± 0.2°C. Control animals were placed in their original location at the normal housing temperature of 22.0 ± 0.2°C. Experimental animals were heated until a T_c of 41.8°C (T_{cMax}) was reached. After attainment of T_{cMax}, rats were removed from the incubator, weighed, placed in a new cage, and returned to normal housing temperature ($T_a = 22.0 \pm 0.2$°C). Time-matched control rats were weighed, provided a new cage, and placed back at their original cage location. Control and experimental animals were provided food and water ad libitum throughout recovery. Body weights were obtained on a top-loading balance with an accuracy of ±0.1 g.

Rat Anatomical Model

The 3-D anatomical model of a rat was acquired from Duke University (49). The model was developed by segmentation and 3-D reconstruction of medical images obtained from MRI based on non-uniform rational B-splines and includes a realistic description of the organs and skeletal system of the rat (Fig. 1). Missing anatomical features, such as the tail, were added to the model by 3-D reconstruction of MR images (81 images, 3-mm thick) obtained from Brooks Air Force Base (58) using the Mimics (Materialise, Plymouth, MI) medical image processing software package. The native format of the anatomical model was the standard stereolithography file format, which describes the surface of geometry using a mesh of triangles. The primary objective of the original anatomical model acquired from Duke University was visualization. Therefore, while the model accurately described the rat anatomy in 3-D, it had artifacts that made it incompatible with the development of a computational model using finite-element method (FEM), especially during the volume mesh generation process. Consequently, the anatomical model was imported into a FEM preprocessor and computer-aided design (CAD) software package, 3-matic (Materialise), and artifacts, such as intersecting organs and bones, were removed. The anatomical model had other artifacts, such as presence of a large number of bad-quality and inverted triangles, and local distortions in the geometry that made it incompatible with the development of a volume mesh for the computational model. These artifacts were removed by local smoothing and meshing of the geometry in 3-matic. The improved surface mesh was then used to create the volume mesh. The mesh consisted of 451,762 tetrahedral volume elements, as shown in Fig. 2. The processed whole body anatomical model included essential organs, such as the heart, liver, kidneys, brain, lungs, stomach, and intestines, as well as the skeletal system. The anatomical model with the mesh was imported into a FEM-based software package, COMSOL Multiphysics (COMSOL, Burlington, MA), to develop the computational model.

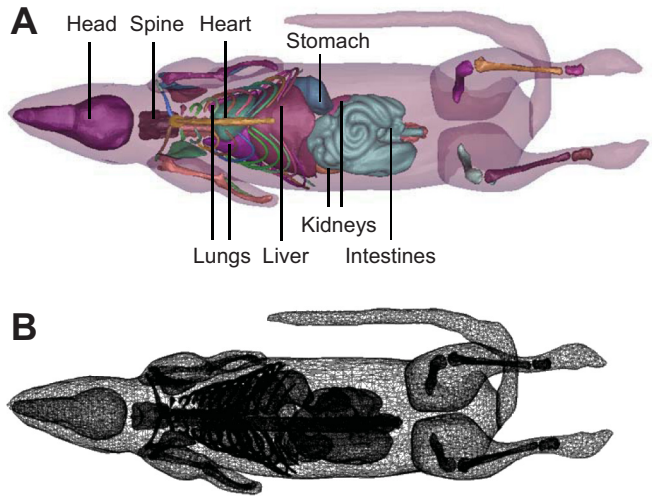

Fig. 2. Geometry (*A*) and mesh (*B*) of the 3-D rat anatomical model. The geometry includes 60 volumes and 70 boundaries representing the organs, interfaces, and external surfaces. The various organs included in the model are shown in different colors. The mesh consists of 451,762 elements.

Computational Model

The physiological model for thermoregulation in rats during heat stress was formulated based on the Pennes bioheat transfer equation (64, 85). The Pennes equation was chosen because it has been successfully employed in numerous whole body human and animal heat transfer models (27, 40, 44). The equation describes the transient change in temperature at any location inside the rat and accounts for heat conduction, heat convection due to blood perfusion in the tissues, and metabolic heat generation. The Pennes equation approximates the heat transfer due to blood perfusion in the body organs as a source (or sink) term instead of explicitly modeling blood flow and heat exchange in the blood vessels, as follows:

$$\rho c_p \frac{\partial T}{\partial t} = \underbrace{\nabla \cdot (k \nabla T)}_{\text{heat conduction}} + \underbrace{\rho_b c_{p,b} \dot{V}_b^v (T_a - T)}_{\substack{\text{heat convection} \\ \text{due to blood perfusion}}} + \underbrace{Q_m}_{\substack{\text{metabolic} \\ \text{heat generation}}} \quad (1)$$

where ρ, c_p, and k denote tissue density, specific heat capacity, and thermal conductivity, respectively; ρ_b and $c_{p,b}$ represent the density and specific heat capacity of the blood, respectively; $\dot{V}_b^v$ denotes the blood perfusion rate in the tissue, and T_a represents the arterial blood temperature.

Circadian variations. Because one of the aims of the model was to predict the temperature distribution in heat-stressed rats during the course of a day, it was critical to incorporate the effects of circadian rhythmicity. Both blood perfusion and metabolic heat generation rates demonstrate circadian variations in rats, as reported in the literature (21, 68, 73, 82). The circadian process for blood perfusion was modeled by implementing the following sinusoidal function:

$$C_{per}(t) = a_{per} \sin\left(\frac{2\pi t}{\tau} + \varphi_{per}\right) \quad (2)$$

where a_{per} denotes the amplitude of circadian variation in blood perfusion, φ_{per} represents the circadian phase, and τ denotes the period of the circadian oscillator (24 h). The amplitude of circadian variation in blood perfusion and the circadian phase for each organ were determined by fitting experimental data on blood perfusion (21)

with *Eq. 2*. The circadian rhythmicity in metabolic heat generation was modeled similarly, as follows:

$$C_{met}(t) = a_{met} \sin\left(\frac{2\pi t}{\tau} + \varphi_{met}\right) \quad (3)$$

where a_{met} denotes the amplitude of circadian variation in metabolic heat generation, φ_{met} represents the circadian phase, and τ denotes the period of the circadian oscillator (24 h). Experimental data on metabolic heat generation (68) were used to obtain the circadian variation and the circadian phase in *Eq. 3*.

Blood flow model. The Pennes bioheat equation (*Eq. 1*) includes the blood perfusion term as a source (or sink) term in the standard heat equation, with the rate of heat transfer between blood and tissue depending on the blood perfusion rate and the difference between arterial blood and tissue temperatures. In this formulation, it is assumed that the heat exchange between blood and tissue takes place in the capillary beds and that the blood equilibrates with the tissue so that the temperature of the blood flowing out of the veins is equal to the local tissue temperature (60). Pennes (64) did not incorporate the subsequent mixing of the venous blood from various organs and tissues in his original work because his model included the forearm only. However, for a whole body model, the arterial blood temperature would depend on the mixing of the venous blood from different tissues before it is pumped back by the heart to the pulmonary and systemic circulations. Incorporating the arterial blood temperature (T_a) as a constant value, as implemented in the original formulation by Pennes (64) and subsequent work (23, 57, 90), can only be justified when modeling a local subsystem of the body (e.g., an arm) or, if modeling the entire body, for only a short duration of heating or cooling, when the global arterial temperature is not expected to change significantly. For whole body thermoregulation models that aim to investigate long-heating periods, as in the proposed work, the assumption of a constant blood temperature is not valid. Therefore, we used a novel mixing formulation for estimating the arterial temperature at any time t, as follows:

$$T_a^t = \frac{\sum_i \int_V \dot{V}_{bi}^v \, T_i^{t-\Delta t} \, dV_i}{\sum_i \int_V \dot{V}_{bi}^v \, dV_i} \quad (4)$$

where the subscript i refers to the various organs included in the model and the time interval (Δt) is the time step size for the computational model. *Equation 4* calculates the volumetric flow-weighted average temperature for the entire body based on the temperature distribution in the body organs at the last computed time step.

Temperature dependence of blood flow. Blood perfusion has been reported to be dependent on temperature, with the rate doubling for each 10°C rise in temperature from the baseline (35). This relationship was implemented in the model using the following equation:

$$\dot{V}_b^v = \dot{V}_{b0}^v \, 2^{\left(\frac{T-T_0}{10}\right)} \quad (5)$$

Equation 5 was successfully used to model human thermoregulation (35), and a modified version of the equation, also derived from human models (5), was used for modeling rats (44).

Additionally, Kregel at al. (51) studied the circulatory dysfunction and observed a differential thermoregulatory response in splanchnic and peripheral blood flows during heat stress. The splanchnic blood flow was observed to decrease during heat stress as opposed to an increase in the peripheral blood flow. In the absence of detailed measurements of changes in blood flow in the different organs due to heat stress, we implemented a linear dependence of blood flows on organ temperatures based on the works of Kregel et al. (51) and Hirata et al. (44), as follows:

$$\dot{V}_{b,HS}^v = \begin{cases} \dot{V}_b^v & T \le T_L \\ \dot{V}_b^v\left[1 + \alpha\dfrac{T - T_L}{T_U - T_L}\right] & T_L < T \le T_U \\ \dot{V}_b^v\left[1 + \alpha\right] & T > T_U \end{cases}$$
$$\dot{V}_{b,HS}^v = \begin{cases} \dot{V}_b^v & T \le T_L \\ \dot{V}_b^v\left[1 - \beta\dfrac{T - T_L}{T_U - T_L}\right] & T_L < T \le T_U \\ \dot{V}_b^v\left[1 - \beta\right] & T > T_U \end{cases} \quad (6)$$

In this formulation, blood perfusion remained at a baseline level below a certain temperature (T_L); linearly increased (in the outer skin layer and tail) or decreased (in the internal organs) with temperature for a fixed temperature range; and remained at an elevated or depressed level after the upper bound temperature (T_U) was reached. *Equation 6* has been previously used for modeling both rat and human thermoregulation (5, 44, 45).

Metabolic heat generation rate. Body organs are known to have significantly different metabolic activity levels. For example, organs such as the liver, brain, kidneys, and heart have been observed to be highly metabolically active compared with other organs and tissues (25, 36, 81). To model the differential thermal response in organs, it is imperative to accurately account for the metabolic heat generation term of each organ. Wang et al. (81) used Kleiber's law (50), which relates the total basal metabolic heat generation rate with body mass, to derive relationships between the basal metabolic rates of different organs and body mass. Metabolic heat generation rates in our model were calculated using these relationships and are listed in Table 1.

Temperature dependence of the metabolic heat generation rate. The metabolic heat generation rate in any organ is a function of biochemical reactions occurring in the cells. This reaction rate doubles for each 10°C rise in temperature from the baseline. Accordingly, the temperature dependence of the metabolic heat generation rate was given by the following (84):

$$Q_m^{organ}(T) = Q_{m0}^{organ} \, 2^{\left(\frac{T-T_0}{10}\right)} \quad (7)$$

Heat generation due to physical activity. Physical activity of the rats inside an incubator was measured by recording the activity count [ac(t)] using radiotelemetry (Fig. 3). Activity count is a relative measure of the distance and speed of movement of the animal. Heat generated due to physical activity was modeled by incorporating the measured activity data in the mathematical formulation. However, since activity count provides only a relative measure of physical activity, the following assumption was employed to quantify the effect of physical activity: because rats inside an incubator were restricted to a light activity level, the maximum measured activity count was assumed to be correlated to the maximum metabolic heat generation rate associated with light activity, as obtained from the literature (1, 8, 9). Subsequently, accounting for the rate of thermal energy generation converted to mechanical power, the following relationship was used to estimate the heat generation rate due to activity in the model (27):

$$Q_{m,activity} = \mathrm{AL} Q_m (1 - \eta)\frac{\mathrm{ac}(t)}{\mathrm{ac}_{\max}} \quad (8)$$

The activity level (AL) for light activity and the corresponding mechanical efficiency in the conversion of metabolic heat into mechanical energy (η) were obtained from the literature and are listed in Table 2. The average measured activity counts [ac(t)] for the control ($n = 30$) and heat-stressed ($n = 50$) rats were calculated (Fig. 3) and input to the model as a function of time.

Table 1. *Thermal and blood flow properties used in the model*

Tissue	Properties, Units						Reference(s)
	ρ, kg/m^3	k, W·m^{-1}·°C^{-1}	c_p, J·kg^{-1}·°C^{-1}	$\dot{V}_{b0}{}^{v}$, m^3·s^{-1}·m^{-3}	a_{per}	Q_{m0}, W/m^3	
Stomach	1,040	0.518	3,500	0.007	0.420	1,837	21, 71, 81
Kidneys	1,040	0.502	3,638	0.107	0.240	38,128	21, 71, 81
Muscle	1,047	0.518	3,500	0.001	0.170	1,849	19, 75, 81
Bone	1,600	0.300	2,000	0.030	0.190	2,826	21, 75, 81
Brain	1,036	0.528	3,854	0.006	0.210	26,351	21, 75, 81
Fat	970	0.204	4,483	0.001	0.570	1,713	19, 75, 81
Heart	1,030	0.526	3,329	0.049	0.200	51,041	21, 75, 81
Liver	1,030	0.511	3,871	0.022	0.200	46,658	19, 75, 81
Lungs	1,040	0.252	1,935	0.253	0.200	1,837	63, 71, 81
Tendon	1,120	0.500	3,118	0.002	0.200	1,978	26, 43, 52, 81
Skin	1,100	0.370	3,700	0.002	0.280	1,943	19, 75, 81
Intestines	1,042	0.518	3,500	0.023	0.200	1,841	21, 75, 81
Blood	1,057		3,600				18

See *Glossary* for definitions.

Heat exchange due to water intake. Rats were freely allowed to drink water kept at room temperature at all times except during heat stress. Accordingly, the heat loss due to this water intake was modeled as a sink term in the Pennes bioheat equation for the stomach, as follows:

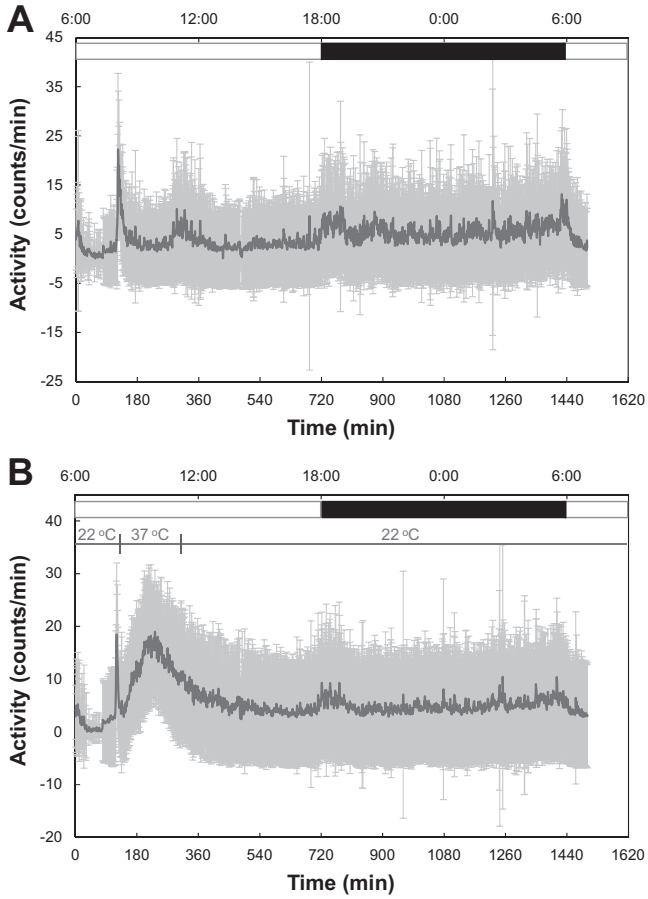

Fig. 3. The relative motor activities of control rats (n = 30) placed at an ambient temperature of 22°C (*A*) and heat-stressed rats (n = 50) in an incubator maintained at 37°C (*B*) for 163 min. The solid lines represent the average of the measured activity values and the gray bars indicate one standard deviation. Motor activity data were used as input parameters to the model to modulate the metabolic heat generation rate. Light and dark cycles are indicated by white and black bars, respectively.

$$Q_{loss} = \frac{m_{water} c_{p,water} \left(T_{water} - T\right)}{\Delta t_{water} V_{stomach}} \quad (9)$$

where m_{water} was the water ingested by the animal as measured in the experiment.

External convection. Under control conditions, rats were kept at normal room temperature and, therefore, their primary mechanism of heat transfer with the surroundings was convection. Similarly, rats were heated by convection due to laminar airflow inside an incubator set at 37°C under heat-stress conditions. Heat transfer due to convection was included in the model as a boundary condition applied to the surface of the rat's skin as follows:

$$-k\frac{\partial T_{skin}}{\partial n} = h_c\left(T - T_{amb}\right) \quad (10)$$

To emulate the experimental conditions for control and heat-stressed animals, different ambient temperatures (T_{amb}) and heat transfer coefficients (h_c) were used, as listed in Table 2. Heat stress in the computational model was prescribed by applying the convective boundary condition for the same application time as per the experimental protocol. Heat transfer coefficients for the control and heat-stress cases were obtained using previously developed correlations available in standard heat transfer literature (48). The corresponding heat transfer coefficients for the head and trunk, forelimbs, hindlimbs, and tail of the rat were obtained using the following equation (48):

$$h_c = \frac{0.683\ \rho^{0.466}\, u^{0.466}\, c_p^{0.333}\, k^{0.667}}{d^{0.534}\, \mu^{0.133}} \quad (11)$$

The characteristic diameters (d) of the various body parts were calculated based on their volumes, and the air properties (ρ, c_p, k, μ) were obtained from the literature (18) for the two ambient temperatures corresponding to control and heat-stress conditions.

Radiation. In addition to convection, the rat's body surface exchanged heat with the surroundings due to radiation. Radiative heat transfer was modeled by applying the following boundary condition on the rat's body surface:

$$-k\frac{\partial T_{skin}}{\partial n} = \varepsilon\sigma\left(T^4 - T_{\text{amb}}^4\right) \quad (12)$$

Evaporative cooling. Due to the absence of sweat glands, rats do not perspire (28). The ability to spread saliva on the surface of their body and the resulting heat transfer due to evaporation is, therefore, a critical heat regulation mechanism for rats. Damas (17) reported that evaporative water loss corresponds to <10% of the total body weight

Table 2. *Input and model parameters in addition to the thermal and blood flow model properties listed in Table 1*

Parameter, Unit	Value	Reference(s)
Input parameters		
Ambient temperature (control condition) (T_{amb}), °C	22	Experiment
Ambient temperature (during heat stress) (T_{amb}), °C	37	Experiment
Water intake ($\dot{m}_{water}$), kg		Experiment
Control conditions	16.47×10^{-3}	
During heat stress	29.38×10^{-3}	
Rate of saliva loss ($\dot{m}_{saliva}$), kg/s		Experiment
Control conditions	4.41×10^{-8}	
During heat stress	2.34×10^{-7}	
Heating time, s	9780	Experiment
Water temperature (T_{water}), °C	22	Experiment
Model parameters		
Reference temperature (T_0), °C	39	44
Specific heat capacity of water ($c_{p,water}$), $J \cdot kg^{-1} \cdot °C^{-1}$	4,180	18
Convective heat transfer coefficient (h_c), $W \cdot m^{-2} \cdot °C^{-1}$		38
Control conditions		
Head and trunk	4.0	
Forelimbs	6.2	
Hindlimbs	4.6	
Tail	9.0	
During heat stress		
Head and trunk	16.2	
Forelimbs	24.9	
Hindlimbs	18.6	
Tail	35.8	
Emissivity (ε), dimensionless	0.8	76
Latent heat of vaporization of water (L_{water}), J/kg	2.26×10^6	18
Activity level for light activity (AL), dimensionless	1.6	1
Mechanical efficiency at light activity (η), dimensionless	0	27
Amplitude of circadian variation in metabolism (a_{met})	0.2	68
Period of the circadian oscillator (τ), s	86,400	21, 68
Circadian phase (φ), dimensionless	0	21, 68

These input and model parameters were either obtained from the literature or were based on the experimental conditions, as noted.

loss in rats at an ambient temperature of 22°C and ~70% for rats heat stressed at 37°C, with urination, defecation, and oxidative metabolism accounting for the remaining weight loss. Accordingly, total body fluid loss due to salivation was estimated based on the total body weight loss of the rats measured during the experiment. The rate of saliva loss was assumed to vary linearly with temperature, as reported in the literature (29, 74). Finally, heat loss per unit area due to salivation was included in the model as the following boundary condition:

$$-k\frac{\partial T_{skin}}{\partial n} = \frac{\dot{m}_{saliva} L_{water}}{A_{rat}} \quad (13)$$

Solution details. The computational model, including the 3-D anatomical model, governing *Eq. 1*, auxiliary equations (*Eqs. 2–9*), and boundary conditions (*Eqs. 10–13*), were set up and solved using the FEM solver, COMSOL Multiphysics. Input and model parameters for the simulations are listed in Tables 1 and 2. Steady-state simulations were performed to initialize the temperature distribution for control and heat-stressed rats at the beginning of the heating protocol. For the steady-state simulation, boundary conditions corresponding to normal room temperature were applied. After the temperature distribution in the computational domain (i.e., the rat geometry) was initialized, time-dependent simulations were carried out to predict temperature distributions over a 25-h time period. Heating conditions corresponding to an ambient temperature of 37°C for 163 min were applied in the model for simulating heat-stressed rats based on the experimental protocol.

RESULTS

Model Validation

The first step in model validation was to compare the model-computed variables with the corresponding data from the literature, as shown in Table 3. However, due to the unavailability of complete anatomical and physiological data for F344 rats, data from various rat strains were used for comparisons. Organ volumes, which were computed by volume integration in the FEM solver, were found to be consistent with those reported in the literature (19, 25, 30, 62, 63, 86), establishing the anatomical accuracy of our model. Subsequently, physiological variables, such as core and organ temperatures and total metabolism and circadian variations, predicted by our model were compared with those reported in the literature, and a fairly good match was observed (Table 3). The most striking features of the comparisons were the accurate predictions of relative temperatures in the

Table 3. *Comparison of our computational model with anatomical and physiological data for normal control rats reported in the literature*

Variable	Model Computed	Experimental Data	Reference(s)
Surface area/body mass, m^2/kg	0.12	0.13	33
Organ volumes, $\times 10^{-6}$ m^3			
Stomach	4.70	1.06–4.58	
Kidneys	2.62	2.00–3.70	
Brain	2.05	1.20–2.07	19, 25, 30, 62, 63, 86
Heart	2.23	1.20–2.35	
Liver	1.04	1.07–1.96	
Lungs	2.93	1.54–2.10	
Intestines	11.50	10.60–15.80	
Core temperature (T_c), °C	37.20	37.0–37.4	33, 68
Circadian variation in T_c, °C	0.80	0.34–1.20	33, 59, 68
Metabolism, W	1.93	1.30–1.99	33, 68
Metabolism, W/kg	6.20	4.5–7.4	33
Circadian variation in metabolism, W	0.77	0.70	68
Organ temperatures compared with blood temperature, °C			
Liver	0.40	0.2–0.3	14, 15
Kidneys	0.20	0.2–0.3	14, 15
Intestines	0.10	0.1–0.13	14, 15
Hindlimbs	−0.50	−0.1 to −0.3	14, 15
Skin	−0.70	−0.6 to −1.2	14, 15
Tail	−12.80	−10.2 to −12.0	34, 70

Surface area and organ volumes were determined by computing the surface and volume integrals of the geometry in the finite-element method solver. Core temperature was calculated using *Eq. 1*. Total metabolism was determined by integrating the metabolic heat generation rate at each point in the geometry, given by the basal metabolic heat generation rate (listed in Table 1) and *Eqs. 3, 7*, and *8*. Organ temperatures were the mean temperatures obtained by calculating the volume-weighted average of the temperature field in each organ given by *Eq. 1*.

organs, which were consistent with published results (14, 15) under normothermic conditions: the liver, kidneys, and intestines were predicted to be at a higher temperature compared with the blood, whereas the hindlimbs, skin, and tail were cooler.

For a quantitative validation of the model dynamics, predicted core temperatures as a function of time of day were compared with those obtained experimentally using radiotelemetry measurements, as shown in Fig. 4. For the control rats, Fig. 4*A* shows that the model predictions were within 1 SD of the measured data ($n = 30$) and accurately captured the amplitude of the circadian rhythmicity in core temperatures during the course of a day-night cycle. Extreme variations in core temperatures (~1.0°C) in control rats close to the start of the experiments (approximately between 0800 and 1100), which could not be captured by the model, were attributed to the external disturbance to the animals due to weighing and removal of food and water at the start of the heating regime and later during refeeding after the heating period (to mimic the disturbances experienced by heat-stressed animals). The predicted core temperature decreased as the day progressed and then peaked during the night with a peak-to-peak amplitude of 0.8°C. However, the model was unable to capture the entire time evolution of the experimental core temperature profile. This may be due to the use of abrupt lights-on and -off transitions to simulate day-night alternation in the experiments, which led to abrupt increases in rat core temperature in anticipation of the lights-off (active) period at 1800. This response is anticipatory of the active period when feeding, grooming, and other behaviors are manifested during the normal circadian cycle. The effect has been extensively studied in the past (69, 77), although in relation to sleep entrainment. The natural day-night transition, however, does not occur abruptly; rather, the light intensity changes continuously throughout the period. Our computational model was unable to mimic the abrupt light and dark transitions and instead incorporated a continuous day-night transition.

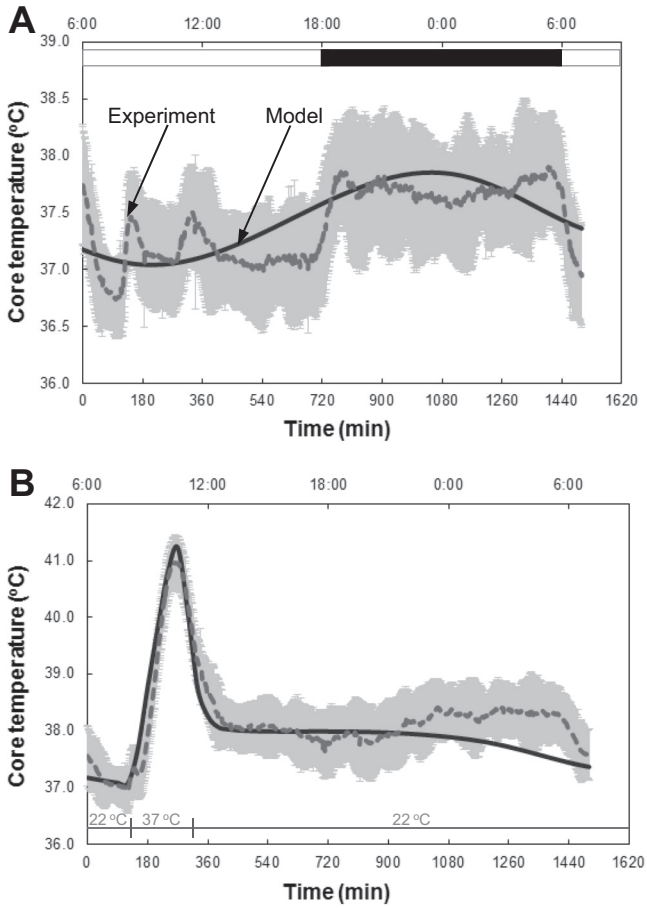

Fig. 4. Model validation using rat core body temperature data obtained from radiotelemetry measurements of control rats ($n = 30$) placed at an ambient temperature of 22°C (*A*) and heat-stressed rats ($n = 50$) in an incubator maintained at 37°C (*B*) for 163 min. The dashed lines represent the average of the measured core temperature values and the gray bars indicate one standard deviation. The core temperatures predicted by our model are plotted by solid lines.

Figure 4*B* shows the comparison of predicted and measured core temperatures for the heat-stressed animals. Again, the model predictions followed the experimental data ($n = 50$) closely, capturing the magnitude of rise in core temperature during heat stress as well as the post-heat-stress temperature response. The maximum rise in temperature due to heat stress was ~4°C. This rise in core temperature was fixed in the experiments since animals were removed from the incubator as soon as they reached a temperature of 41.8°C. The computational model precisely predicted the timing and amplitude of the temperature rise, which were not fixed in the simulations because the model input boundary conditions only included the measured time-dependent temperature profile in the incubator, ranging from 22°C to 37°C (per the experimental protocol), thereby further validating the model predictions. After the removal of heat stress (at ~1045), the core temperature started to fall rapidly but remained ~1.0°C higher in heat-stressed rats compared with control rats even after 110 min of cooling. A delayed nighttime circadian rise in temperature was observed in the measured data but was not captured by the simulations.

Spatial Temperature Distribution

Figure 5 shows the predicted spatial temperature distribution in control (Fig. 5*A*) and heated (Fig. 5*B*) rats at the time when the core temperature reached its peak value in the heated animal. In Fig. 5, *A* and *B*, different color scales for temperature were used to illustrate the temperature nonuniformity in different organs. For the control rat (Fig. 5*A*), the temperature profile on the skin surface (left panel) was fairly uniform except in the tail, where lower temperatures were observed. The average tail surface temperature of 24.3°C was significantly lower than the average skin temperature (excluding the tail) of 36.5°C, as corroborated by previously published experimental data (41, 70, 78). The extremities, forelimbs at an average temperature of 35.7°C and hindlimbs at 36.0°C, were also cooler than other regions of the body surface (36.7°C). The temperature distribution for the inner organs (Fig. 5*A*, right panel) shows comparatively higher temperatures in the liver and head regions. In the skeletal system, the bones in the forelimbs (humerus, radius, and ulna) and those in the hindlimbs (femur, tibia, and fibula) were found to be at a lower temperature compared with the vertebrae and ribs.

For the heat-stressed rat (Fig. 5*B*), there was a marked difference in temperatures on the tail surface compared with other locations on the body surface (left panel), similar to the control rat. However, the magnitude of temperature difference

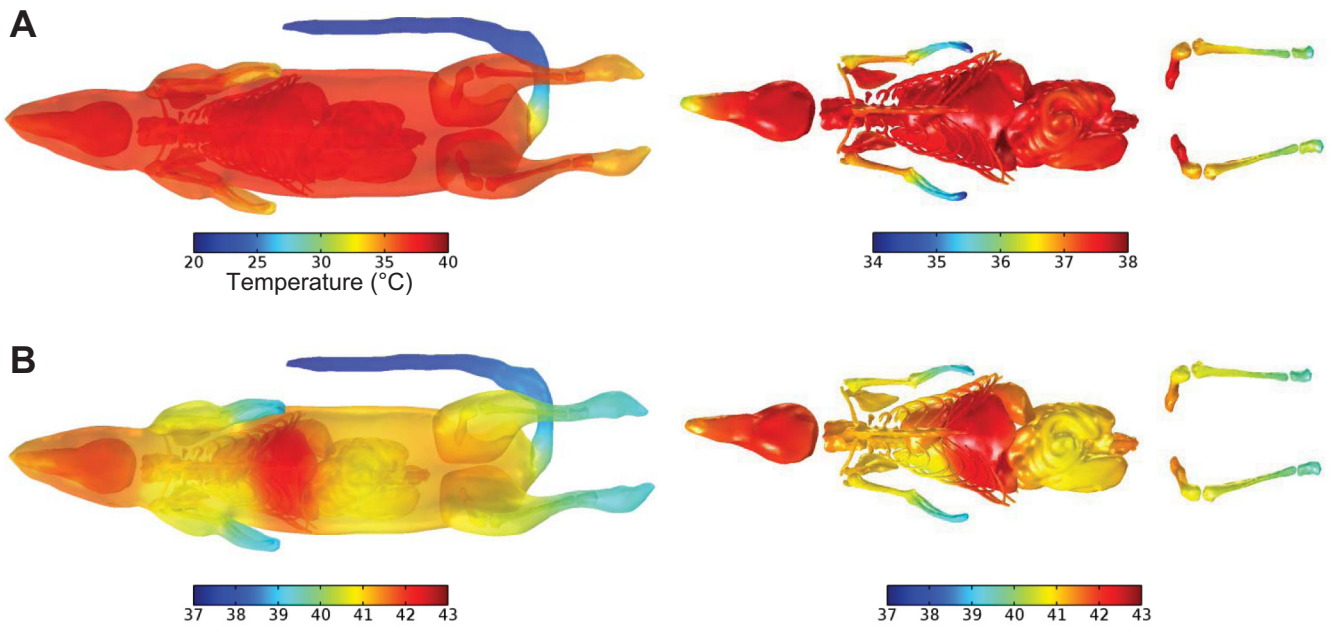

Fig. 5. Predicted spatial temperature distribution at time = 4.75 h from the start of the simulations (when the predicted core body temperature of the heat-stressed rat reached its maximum value) in the control (*A*) and heat-stressed rats (*B*). In *A* and *B*, different color scales were used to illustrate the spatial temperature distribution across the various organs. *Left*: skin surface temperatures; *right*: internal organ temperatures.

was significantly smaller, 1.7°C as opposed to 12.2°C in the control rat. Likewise, the forelimbs and hindlimbs were also at a lower temperature than the other regions of the body surface. The most critical observation from the temperature distribution in the inner organs of the heat-stressed rat (Fig. 5*B*, right panel) was the occurrence of considerably higher temperatures in the liver. This result provides an indication of the increased susceptibility of the liver to heat injury. The lower ribs also had higher temperatures compared with other bones due to their proximity to the liver. Furthermore, temperatures in the head and heart were also higher than other organs. Although the model predictions provide critical insights about the expected temperature distribution in the different organs during heat stress, it is important that these predictions are experimentally validated in the future.

Thermoeffector Responses to Heat Stress

Figure 6 shows the contribution of the major heat transfer mechanisms in the control and heat-stressed animals at the time corresponding to the observance of peak core temperature and immediately after the removal from heat stress. Heat loss due to convective heat transfer with the surroundings decreased during heat stress as the incubator temperature was higher compared with the control ambient condition (37°C vs. 22°C). Immediately after the animal was placed at room temperature (22°C), convective heat loss from the animal increased due to a larger temperature difference, which accelerated cooling. Similarly, heat was lost due to increased evaporation during heat stress, which was sustained even after heat stress. Heat generated due to metabolism increased in the animal during heat stress due to an increase in whole body temperatures (Fig. 5*B*). Blood flow contributed to an increase in heat transfer during heat stress. However, after the removal of heat stress, blood circulation facilitated cooling in the animal.

The Heat-Stress Response in the Organs

Temperature variations in the organs computed by the model were plotted as a function of time to study the differential heat-stress response and are shown in Fig. 7. The temperatures shown in the plot are volume-weighted average temperatures in the entire organ and not the maximum temperature at a single location inside the organ, thereby providing an index for overall heat load to a particular organ. The highest predicted temperatures were observed in the liver, followed by the brain, stomach, and heart. The temperatures in these organs (solid lines) were consistently higher than the core temperature (dashed lines) throughout the day-night cycle. The difference between the maximum temperatures in these organs and the core were 1.2, 0.8, 0.4, and 0.4°C for the liver, brain, stomach,

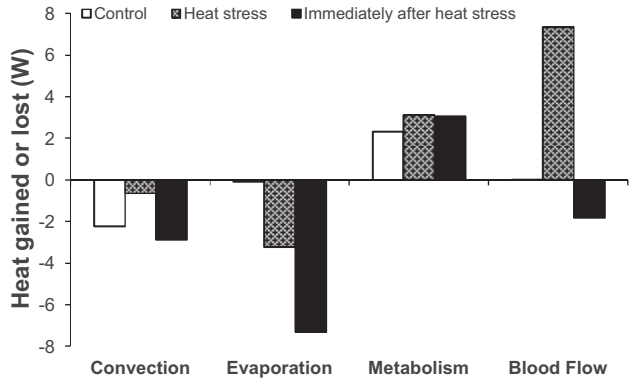

Fig. 6. Contribution of major heat transfer mechanisms computed by the model in the control and heat-stressed animals at time = 4.75 h from the start of the simulation (corresponding to the observance of peak core temperature) and for the time immediately after heat stress (exposed animals only). Positive values indicate heat gained by the animal, whereas negative values denote heat lost by the animal.

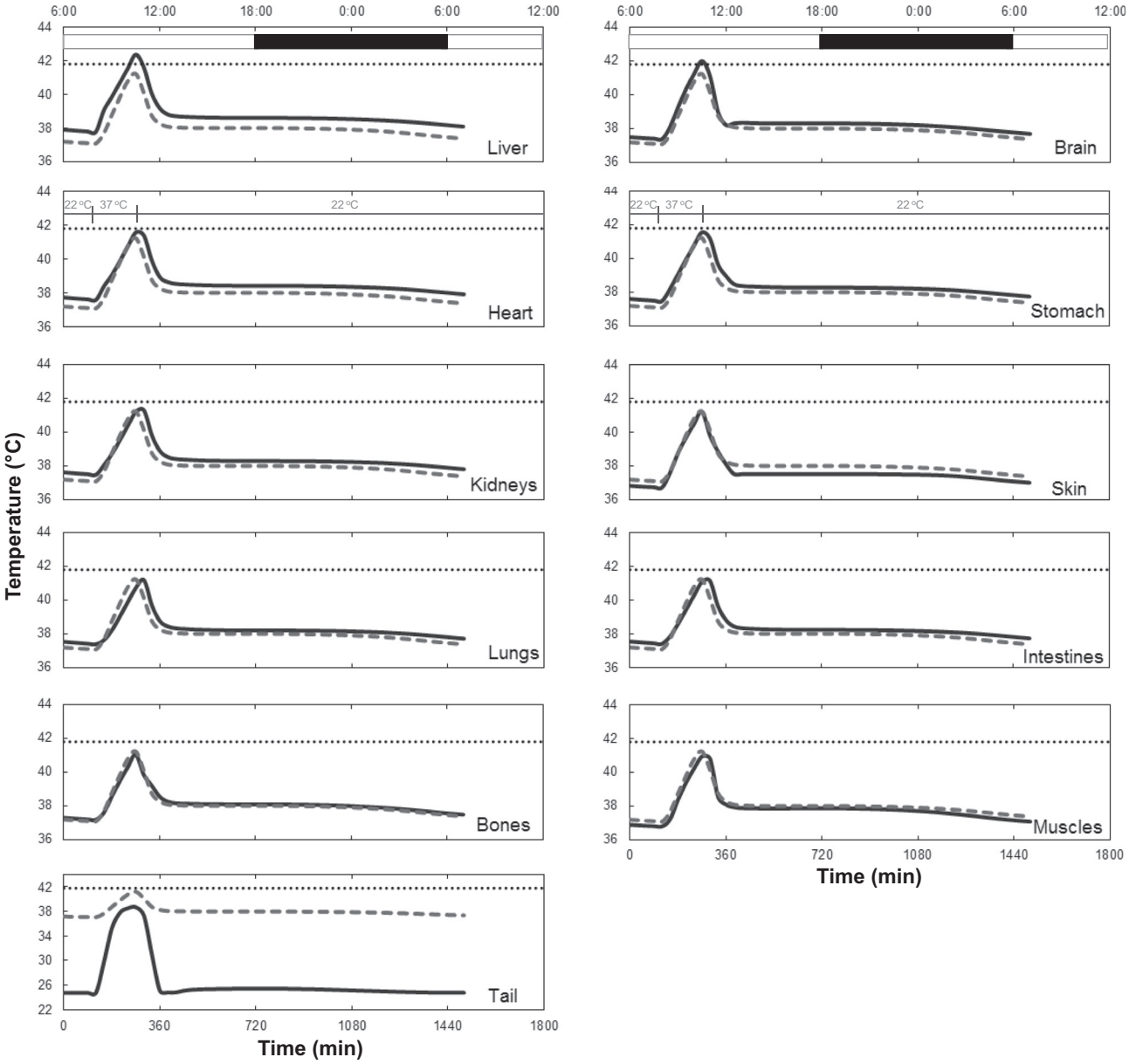

Fig. 7. Differential thermal responses in various organs (solid lines) compared with the core temperature response (dashed lines). The horizontal dotted line in each plot indicates a temperature of 41.8°C, the temperature to which the core was restricted in the experiments. The plots are ordered from highest (*top*) to lowest (*bottom*) organ temperature.

and heart, respectively. The kidneys, lungs, and intestines were nearly at the same temperature as the core, with the difference in peak temperatures being <0.1°C. The average temperature in the tail remained considerably lower than the core temperature for the entire duration of the day-night cycle. Peak temperatures for all organs were observed at the same time as the core except for the kidneys, lungs, and intestines, which were out of phase with a delay of ~30 min.

To compare the thermal response in heat-stressed rats with controls, the difference in average peak temperature in the various organs was calculated and is shown in Table 4. Average peak temperature was defined as the mean temperature in an organ at the time when the highest temperature was observed in that organ during the heat-stress condition. The temperature difference in each organ was calculated by determining the average peak temperature in the heat-stress condition and subtracting it by the corresponding average temperature in the same organ at the same instant of time in the control rat. The highest rise in temperature was observed in the tail, which was more than three times the rise in core temperature (13.7°C vs. 4.2°C). There was also a significant rise in temperature in the liver and brain, while the stomach exhibited an equal rise in temperature compared with the core. For all other organs, the increase in temperature due to heat stress was lower than that in the core. The lowest increase in temperature was observed in the blood.

To test the robustness of our model predictions, we performed simulations for a range of incubator temperatures (37.0 ± 1.0°C) in the vicinity of the actual experimental temperature (37.0°C) used to induce heat stress in the animals. These simulations also

Table 4. *Statistics of the predicted heat-stress responses in the various organs*

Location	Average Peak Temp, °C	Increase in Average Peak Temp vs. Control, °C	Maximum Temp, °C	Organ Volume Fraction with $T > 41.8$°C, %
Liver	42.4	4.7	42.9	95.6
Brain	42.0	4.6	42.2	91.2
Stomach	41.6	4.2	42.3	12.1
Heart	41.6	4.1	42.2	15.5
Kidneys	41.3	3.9	41.9	0.2
Core	41.2	4.2	41.2	
Lungs	41.2	3.9	41.6	0.0
Intestines	41.1	3.8	42.0	0.4
Bone	41.0	3.9	42.4	2.6
Blood	40.4	3.1	40.4	
Tail	38.5	13.7	40.7	0.0

Average peak temperature was defined as the mean temperature in an organ at the time when the highest temperature was observed in that organ during heat stress. Maximum temperature corresponded to the highest temperature at any location in an organ during heat stress. The organs in the table are ordered from highest (top) to lowest (bottom) organ temperature.

tested any potential effect that the precision (±0.2°C) of the incubator temperature sensor could have in the predicted organ temperatures. Figure 8 shows organ-averaged temperature changes in the different organs relative to the core temperature for incubator temperatures of 36.0, 36.8, 37.0, 37.2, and 38.0°C. The model predicted that the highest temperatures occurred in the liver for all cases, followed by brain and stomach. In addition, we found that the organs had the same heat load relative to each other in all simulations.

Average temperature rise provides an index of the heat-stress response for the overall organ. However, during heat stress, there may be locations inside the organs that may be at a considerably higher temperature than the average value. These regions may be more susceptible to post-heat-stress disorders compared with other locations in the organ and, therefore, identification of these "hot spots" is critical. The computed maximum temperatures inside each organ are shown in Table 4. The maximum temperatures in each organ, except for the tail, were higher than the core temperature. For example, in the liver, the maximum temperature reached 2°C higher than the measured core temperature. In addition to the liver, brain, heart, and stomach, which had average temperatures higher than the core, other organs that had average temperatures similar to that of the core, such as the kidneys, lungs, intestines, and some bones, also had hot spots that exceeded the observed core temperature. In certain organs, such as the intestine, a significantly higher maximum temperature compared with the average temperature was observed.

The portion of an organ reaching a temperature greater than the lethal temperature for the species could also be an important quantitative indicator of the heat-stress response. The lethal core temperature for rats has been reported to be in the range of 42.5°C to 44.8°C (33). In this work, the core temperature was restrained to 41.8°C to limit animal mortality during the course of the experiment. Therefore, to quantify the heat load in each organ, calculations were performed using the computational model to determine the volume fraction of the organs reaching the limiting temperature of 41.8°C or higher. The volume fractions are shown as percentages in Table 4. As expected, and in agreement with other measures of the heat-stress response discussed above, the liver and brain showed the greatest susceptibility to heat load, with >90% of these organs reaching a temperature ≥41.8°C. In contrast, 10–15% of the heart and stomach also attained temperatures ≥41.8°C. Other organs had negligible percentages of their volumes reaching the limiting temperature.

DISCUSSION

In this study, we developed an anatomically accurate computational model for thermoregulation in rats during heat stress and compared the heat-stress response with the control condition. The novelty of this work stems from the comprehensive description of various heat transfer mechanisms and incorporation of an accurate representation of the rat anatomy to demonstrate that monitoring the differential thermal response in each body organ is critical to assess the actual condition of the animal during heat stress. While anatomically accurate computational models have been developed for thermoregulation in rats (44, 71, 75), the aims of these studies were to investigate the effects of electromagnetic radiations over short intervals of time (30–5,400 s) and, therefore, did not have to consider certain key phenomena with long periodicity. In addition, these studies did not investigate the differential thermal response in the organs, which can potentially lead to distinct severity of organ dysfunction during severe heat stress. A comprehensive model for describing the differential heat-stress response for an entire day-night cycle has not been previously reported.

Mechanistic models, such as the one developed in this work, are models that incorporate and enable understanding of the underlying biological processes and, therefore, provide predictive capability over a wide range of conditions. A critical

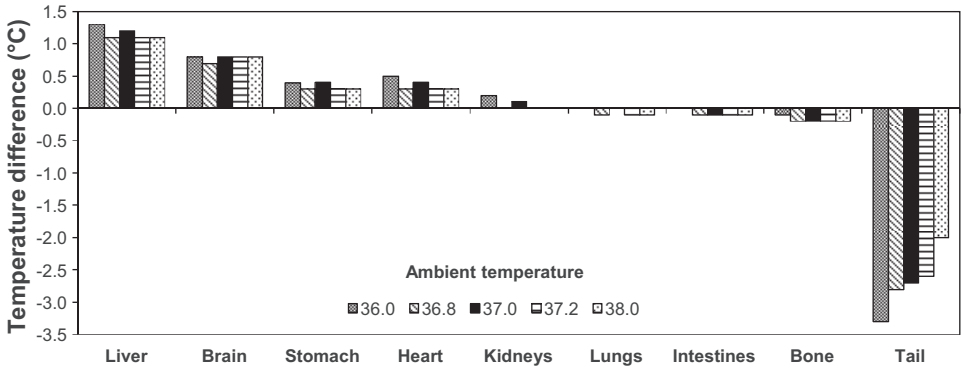

Fig. 8. Organ-averaged temperature changes relative to the core temperature for five simulations of incubator temperatures ranging from 36°C to 38°C. Positive values indicate higher average organ temperature compared with the core, whereas negative values denote lower organ temperature.

element in the development of mechanistic models, which has been lacking in similar applications (71, 75), is a detailed model validation procedure using in vivo experimental data. In some studies (40), the same set of experimental data was used for estimating the model parameters and validating the model predictions, which limits the applicability of the model to "fit" the observed conditions. In contrast, in our model validations, we compared our model predictions with extensive independent experimental data, thereby retaining the mechanistic nature of the model for making predictions beyond the observed conditions. The experimental data used for model validation were not used to estimate the model input parameters. We used a large number of animal experiments to quantify the average thermal response of both heat-stressed animals ($n = 50$) and control animals ($n = 30$) and compared them to the model predictions (Fig. 4). Moreover, additional published data were used to corroborate the accuracy of the model predictions of certain physiological variables (Table 3).

Physiologically, the temperature of the blood is a function of the environmental conditions and heat transfer characteristics similar to any other tissue or organ in the body. However, in a large number of computational models used to predict temperature distribution, blood temperature is assumed to be a constant (23, 40, 57, 71, 75, 90). This assumption may only be valid for cases when a portion of the body is being heated and the overall temperature changes in the body may be considered insignificant. When the aim of the model is to study the thermoregulation in body organs over a period of time, it is critical to consider changes in blood temperature as a function of temperature changes in other organs. Otherwise, the model formulation would artificially introduce a source (or sink) term for generation (or loss) of heat due to the assumption of constant blood temperature, which is not physiological. Our model accounts for this change in blood temperature using a novel methodology, which incorporated the mixing of blood from various organs, and is therefore able to more accurately capture the experimental observations.

Even at an ambient temperature of 22°C, at which rats demonstrate normothermic core temperatures (33), there is substantial variation in temperature distribution in the different organs (14, 15, 34, 70). To accurately study the resulting dynamics of evolution of temperature profiles in the organs due to subsequent heat stress, it is important to start with the correct normothermic response. Consequently, it is critical that the model simulations of the steady-state baseline conditions are capable of predicting the normothermic temperature distribution as opposed to having to provide the starting temperature distribution as an initial condition. This not only ensures that the model is initialized in a physiologically correct manner, which can be validated, but also justifies the selection of input parameters and heat-transfer mechanisms for the model. Although some of the published models have used steady-state simulations to initialize the model and predict the baseline response (75, 76), a majority have used either a uniform temperature distribution for the entire body as the initial condition (40) or a steady-state simulation-based temperature distribution that was not validated (27). In our modeling framework, we predicted the temperature distribution in normothermia as the result of a steady-state simulation and compared the predictions with published physiological data.

Past studies have emphasized the need to characterize heat transfer in the rat's tail in detail because of its role in facilitating heat loss during heat stress (67, 78, 87). The tail, owing to its large surface area and an enhanced blood supply, can easily exchange heat with the surroundings by convection and radiation (20). The tail, therefore, serves as an important organ in thermoregulation, vasodilating blood vessels to permit increased blood perfusion for greater cooling during heat stress and vasoconstricting them to minimize heat loss when placed in a cold environment. Although these features have been implemented in stand-alone models for tail thermoregulation (67, 87), whole body models have not accounted for these additional heat transfer mechanisms (40, 75). The change in heat transfer characteristics in the tail at different ambient temperatures is primarily attributed to the change in convective heat transfer and rate of blood perfusion. These mechanisms were incorporated in our model, and, consequently, we could more accurately capture the temperature distribution in the tail at normal ambient temperature as well as during heat stress. Our model predicted that convection was the dominant mechanism of heat transfer in the tail (results not shown).

In addition to significant difference in temperature distribution in the different organs at any given time, the temperatures in the organs also change during the day-night cycle due to circadian rhythmicity. Metabolic heat generation and blood perfusion have been known to demonstrate circadian variations (21, 68). This work is the first attempt to predict the circadian changes in temperatures using a mechanistic whole body model. Our model accurately captures the nocturnal characteristic in the circadian variation of temperature with higher nighttime temperatures compared with daytime temperatures. Incorporation of this circadian rhythm is important in the context of heat stress because, compared with the rise in temperature during stress (~4°C), the circadian variation in temperature is appreciable [~0.8°C for this study, but higher (1.2°C) in previous reports (33, 59, 68)]. The extent of heat injury, therefore, depends not only on the external temperature but also on the time of day it is initiated, as even a lower ambient temperature may elicit a similar thermal response if applied at a different time during the day. Preclinically, the model can be used to design optimized heating experiments to elicit desired responses in animals to study heat-stress progression.

The dynamics of temperature changes during heat stress is a result of complex interplay of anatomy, tissue properties, and external and internal heat-transfer mechanisms. As the ambient temperature increases, temperatures at the rat's skin surface start to rise due to increased convective heating (Fig. 4*B*). Heat is subsequently transferred to the internal organs by conduction and convection due to blood perfusion. Conduction is, in turn, dependent not only on the characteristics of the particular tissue but also on the anatomical placement of the organ, and, therefore, organs farther away from the skin surface are heated later, generating a temperature gradient in the body. Conversely, convective heat transfer due to blood flow is much faster and tends to equilibrate the temperatures in the different organs. The rate of convective heat transfer corresponds to the temperature-dependent blood perfusion rate in the particular organ. Moreover, different organs have varied metabolic heat generation rates, which themselves change due to change in temperatures. At the same time, heat is lost from the skin

surface due to evaporation of saliva. All these mechanisms of heat transfer make the process highly nonlinear with respect to any variable, e.g., although the heart has the highest metabolic heat generation rate (Table 1), it does not reach the highest temperature due to the combined effect of all other heat-transfer mechanisms. The computational model incorporates the various phenomena involved in the heat-stress process necessary for predicting the temperature responses, as shown in Figs. 4, 5, and 7, and enabling us to tease out the key heat-transfer mechanisms (Fig. 6). The temperature rise in most organs is in phase (Fig. 7), possibly because heat transfer due to blood perfusion is the dominant mode of heating. Heat conduction also plays an important role, as can be observed by the temperature variations within an organ (Fig. 5*B* and Table 4). For organs, such as lungs and kidneys, which reach the maximum temperature after a delay (Fig. 7), conduction is the more significant heat-transfer mechanism.

The most powerful contribution of the model is its capability to provide a framework for comprehensive whole body prediction of temperature changes. The model results show that certain organs attain much higher peak temperatures compared with the core (Table 4). Measuring only the core or rectal temperature, as routinely done in heat-stress studies (7, 54, 88), may not present an accurate picture of the thermal response in the entire body. Additionally, significant differences in temperature distribution can be observed even for organs in close proximity to each other (Figure 5*B* and Table 4). Therefore, irrespective of where the temperature measurement is done, it is critical to consider the spatial variation of temperature in other organs. Another drawback of measuring only the core temperature, or the temperature at a specific location in an organ, is that it does not provide insights about the possible presence of "hot spots" or regions of high temperatures within an organ. Our model demonstrates (Table 4) that there may be locations within an organ that may achieve considerably high temperatures even though other regions in the organ may be well below the lethal temperature. This, in turn, makes analysis of spatial temperature distribution all the more essential. Although imaging techniques, such as MRI-based thermometry, have been used for two-dimensional spatial monitoring of temperature changes in specific organs during thermal therapy of short durations (2, 66), live monitoring of 3-D temperature distributions in the entire body in large groups of animals in a heat-stress study is still not feasible. Therefore, with the limited availability of experimental methods, our computational model nicely complements core temperature measurement experiments in providing an estimate of the temperature distribution in the entire body during heat stress.

The most critical finding from our work is that, among the organs, the liver experiences the highest temperatures during heat stress (Table 4). The brain reached the second highest temperatures following the liver. Based on the expected temperature elevation in the various organs predicted by our model, appropriate cooling strategies could be used for specific organs. Furthermore, histopathology studies of heat-stressed animals have shown progressively greater organ damage associated with higher temperatures (56). Liver dysfunction has indeed been reported to occur early in heat stroke (31, 83). Moreover, cerebral ischemia, injury, and dysfunction during heat stroke have also been reported in the literature (12, 13). While further experiments and analyses are needed to directly correlate the subsequent inflammatory response and MODS with temperature distribution in the organs, the model provides a reasonable estimate of the susceptibility of a particular organ for dysfunction as a result of heat stress.

Although our model includes a comprehensive array of heat-transfer mechanisms involved during thermal stress in rat, thermoregulation is a complicated process, and it is not possible to replicate all mechanisms involved in a living organism. Another limitation is that assumptions were made throughout the model formulation stage. For example, heat transfer due to blood perfusion was simplified by using the Pennes bioheat transfer equation and by employing a mixing formulation for change in blood temperature. Nevertheless, the model was extensively validated using in vivo experimental data to justify these and other model assumptions as well as the selection of the key heat-transfer mechanisms. Moreover, no ad hoc model input parameters were used, so the model remains mechanistic in nature.

The progression of heat stroke from the temperature rise in the body to inflammation and MODS is a complex process. Our model aims at investigating only the initial phase of this cascade of events. However, to model the entire pathophysiology, it is important not only to include the physiological events (temperature change) but also the resulting biological response (inflammation). For example, the feverlike response in core temperature after an initial temperature rise cannot be predicted mechanistically by the model without incorporating the effects of biological factors, such as the role of cytokines (53), activated as a result of heat injury. However, as with any computational model, to incorporate these relationships in a model, it is important to first study them experimentally. A detailed experimental animal model is, therefore, needed to clearly elucidate the relationship between the temperature rise in each organ and the resulting change in inflammatory mediators before such a molecular computational model can be envisioned. Nevertheless, our present model provides a starting point for the development of such a multiscale, molecular-physiological computational model for heat stroke.

Monitoring of organ temperatures is not a trivial endeavor in a conscious rodent model because multiple transmitters cannot be implanted into the peritoneal cavity of an animal (large size precludes this) and regional differences within an organ would need to be considered as well. However, brain (e.g., hypothalamic, cerebellum) temperature could be simultaneously monitored with the core temperature. It might also be possible to monitor individual organ temperatures under anesthetized conditions. Presumably, with advancements in radiotelemetry (i.e., smaller transmitter size and elimination of frequency interference among devices) and imaging technologies, it may be possible to validate organ-specific temperature predictions in the near future. Alternatively, one could take a more simple approach of rapidly sacrificing animals and measuring organ temperature in situ at different times during recovery to validate the model predictions, although with limited accuracy.

The ability to predict the spatio-temporal temperature distribution opens opportunities for potential clinical and design applications. Because the model is mechanistic, it can be used for simulating a multitude of "what-if" scenarios of different heat-stress episodes to design optimized experimental protocols. This would help in substantially reducing the number of animals required for such experimentations. The model could also be used to test and design novel heat stress management

techniques, such as localized cooling. Brain cooling has shown promise in the recovery from heat stroke in rats (47), and similar localized cooling techniques could be used for inducing hypothermia in other heat-stroke-susceptible organs, such as the liver (31, 83). Further, the spatial temperature distribution in the various organs could be used to anchor and analyze molecular mediators of heat injury in an organ-specific manner, in particular in relation to hot spots. This, in turn, would help in the identification of predictive and diagnostic biomarkers of systemic inflammation and organ injury after heat stress. If imaging techniques, such as MRI, are used to estimate tissue damage during heat-stress recovery, it may be possible to determine the effect of different predicted organ temperatures on the progression of organ damage. Finally, the model could also be used to simulate the efficacy of preventative measures, such as customized apparel, for limiting heat-stress occurrences.

In summary, our model is successfully able to predict the thermal response in rats during heat stress. We used the model results to demonstrate that monitoring the spatial distribution of temperature during heat stress is critical. The model results can be used to quantify the heat load in various organs by determining indices, such as average temperature rise, maximum temperature, and volume fraction of organ reaching the fatal temperature, which may not be possible to experimentally measure. The model, therefore, complements experiments and can be used for further understanding the complex processes involved in thermoregulation in rats. Finally, the model enables identification of organ-specific risks during heat stress, which will potentially aid in the development of improved clinical strategies for injury prevention and management.

ACKNOWLEDGMENTS

We thank Dr. Patrick A. Mason (Office of the Director of Assistant Secretary of Defense for Research and Engineering), Dr. John Ziriax (Naval Surface Warfare Center Dahlgren Division), and Dr. W. Paul Segars (Duke University Medical Center) for sharing the initial rat anatomical models. We also thank Shauna Dineen, Rocio Duran, Michael Blaha, and SGT Jermaine Ward for invaluable technical assistance with the rat heat-stress experiments. We thank Dr. Alexander Mitrophanov for the discussion regarding sensitivity analysis.

The opinions and assertions contained herein are the private views of the authors and are not to be construed as official or as reflecting the views of the U.S. Army or of the U.S. Department of Defense. This paper has been approved for public release with unlimited distribution.

In conducting the research described in this report, the investigators adhered to the "Guide for Care and Use of Laboratory Animals" as prepared by the Committee on Care and Use of Laboratory Animals of the Institute of Laboratory Animal Resources, National Research Council.

GRANTS

The research was supported by the U.S. Army Network Science Initiative and the Military Operational Medicine Research Program, U.S. Army Medical Research and Materiel Command, Ft. Detrick, Maryland.

DISCLOSURES

No conflicts of interest, financial or otherwise, are declared by the author(s).

AUTHOR CONTRIBUTIONS

Author contributions: V.R., J.D.S., B.G.H., L.R.L., D.A.J., and J.R. conception and design of research; B.G.H. and L.R.L. performed experiments; V.R. developed model and performed simulations; V.R. and J.D.S. interpreted results of simulations; V.R., B.G.H., and L.R.L. drafted manuscript; J.R. edited manuscript; V.R., J.D.S., B.G.H., L.R.L., D.A.J., and J.R. approved final version of manuscript.

REFERENCES

1. **ANSI 55–2004/ASHRAE.** *Thermal Environmental Conditions for Human Occupancy*. Atlanta, GA: American Society of Heating, Refrigerating and Air-Conditioning Engineers, 2004, p. 15–17.
2. **Abe H, Kurumi Y, Naka S, Shiomi H, Umeda T, Naitoh H, Endo Y, Hanasawa K, Morikawa S, Tani T.** Open-configuration MR-guided microwave thermocoagulation therapy for metastatic liver tumors from breast cancer. *Breast Cancer* 12: 26–31, 2005.
3. **Argaud L, Ferry T, Le QH, Marfisi A, Ciorba D, Achache P, Ducluzeau R, Robert D.** Short- and long-term outcomes of heatstroke following the 2003 heat wave in Lyon, France. *Arch Intern Med* 167: 2177–2183, 2007.
4. **Armed Forces Health Surveillance Center.** Heat injuries, active component, U.S. Armed Forces, 2011. *Med Surv Monthly Report (MSMR)* 19: 14–16, 2012.
5. **Bernardi P, Cavagnaro M, Pisa S, Piuzzi E.** Specific absorption rate and temperature elevation in a subject exposed in the far-field of radio-frequency sources operating in the 10–900-MHz range. *IEEE Trans Biomed Eng* 50: 295–304, 2003.
6. **Bouchama A, Knochel JP.** Heat stroke. *N Engl J Med* 346: 1978–1988, 2002.
7. **Bouchama A, Roberts G, Al Mohanna F, El-Sayed R, Lach B, Chollet-Martin S, Ollivier V, Al Baradei R, Loualich A, Nakeeb S, Eldali A, de Prost D.** Inflammatory, hemostatic, and clinical changes in a baboon experimental model for heatstroke. *J Appl Physiol* 98: 697–705, 2005.
8. **Bramante PO.** Energy metabolism of the albino rat at minimal levels of spontaneous muscular activity. *J Appl Physiol* 24: 11–16, 1968.
9. **Bramante PO.** Quantitation of oxygen consumption and spontaneous muscular activity of the rat. *J Appl Physiol* 16: 982–990, 1961.
10. **Carter R 3rd, Cheuvront SN, Williams JO, Kolka MA, Stephenson LA, Sawka MN, Amoroso PJ.** Epidemiology of hospitalizations and deaths from heat illness in soldiers. *Med Sci Sports Exerc* 37: 1338–1344, 2005.
11. **Casa DJ, Armstrong LE, Ganio MS, Yeargin SW.** Exertional heat stroke in competitive athletes. *Curr Sports Med Rep* 4: 309–317, 2005.
12. **Chang CK, Chang CP, Chiu WT, Lin MT.** Prevention and repair of circulatory shock and cerebral ischemia/injury by various agents in experimental heatstroke. *Curr Med Chem* 13: 3145–3154, 2006.
13. **Chen YC, Liu YC, Yen DH, Wang LM, Huang CI, Lee CH, Lin MT.** L-Arginine causes amelioration of cerebrovascular dysfunction and brain inflammation during experimental heatstroke. *Shock* 29: 212–216, 2008.
14. **Closa D, Alemany M, Remesar X.** Effect of cold-exposure on organ temperatures in Wistar and Zucker *fa/fa* rat. *J Therm Biol* 17: 83–88, 1992.
15. **Closa D, Gomez-Sierra JM, Latres E, Alemany M, Remesar X.** Short-term oscillations of aortic core temperature and thermogenic organ blood flow in the rat. *Exp Physiol* 78: 243–253, 1993.
16. **Damanhouri ZA, Tayeb OS.** Animal models for heat stroke studies. *J Pharmacol Toxicol Methods* 28: 119–127, 1992.
17. **Damas J.** Water losses induced by heat exposure and the kinin system in the rat. *Arch Int Physiol Biochim Biophys* 101: 227–232, 1993.
18. **Datta AK, Rakesh V.** *An Introduction to Modeling of Transport Processes: Applications to Biomedical Systems*. Cambridge, UK: Cambridge University Press, 2009, p. 427–444.
19. **Davies B, Morris T.** Physiological-Parameters in Laboratory-Animals and Humans. *Pharmaceut Res* 10: 1093–1095, 1993.
20. **Dawson NJ, Keber AW.** Physiology of heat loss from an extremity: the tail of the rat. *Clin Exp Pharmacol Physiol* 6: 69–80, 1979.
21. **Delp MD, Manning RO, Bruckner JV, Armstrong RB.** Distribution of cardiac output during diurnal changes of activity in rats. *Am J Physiol Heart Circ Physiol* 261: H1487–H1493, 1991.
22. **Diller KR, Hayes LJ.** A finite element model of burn injury in blood-perfused skin. *J Biomech Eng* 105: 300–307, 1983.
23. **Elwassif MM, Kong Q, Vazquez M, Bikson M.** Bio-heat transfer model of deep brain stimulation-induced temperature changes. *J Neural Eng* 3: 306–315, 2006.
24. **Epstein Y, Roberts WO.** The pathopysiology of heat stroke: an integrative view of the final common pathway. *Scand J Med Sci Sports* 21: 742–748, 2011.
25. **Even PC, Rolland V, Roseau S, Bouthegourd JC, Tome D.** Prediction of basal metabolism from organ size in the rat: relationship to strain, feeding, age, and obesity. *Am J Physiol Regul Integr Comp Physiol* 280: R1887–R1896, 2001.

26. **Farris DJ, Trewartha G, McGuigan MP.** Could intra-tendinous hyperthermia during running explain chronic injury of the human Achilles tendon? *J Biomech* 44: 822–826, 2011.
27. **Fiala D, Lomas KJ, Stohrer M.** A computer model of human thermoregulation for a wide range of environmental conditions: the passive system. *J Appl Physiol* 87: 1957–1972, 1999.
28. **Furuyama F, Murakami M, Oiwa T, Nishino H.** Differences in thermal salivation between the FOK rat (a model of genotypic heat adaptation) and three other rat strains. *Physiol Behav* 63: 787–793, 1998.
29. **Furuyama F, Murakami M, Tanaka E, Hida H, Miyazawa D, Oiwa T, Isobe Y, Nishino H.** Regulation mode of evaporative cooling underlying a strategy of the heat-tolerant FOK rat for enduring ambient heat. *Am J Physiol Regul Integr Comp Physiol* 285: R1439–R1445, 2003.
30. **Gajsek P, Ziriax JM, Hurt WD, Walters TJ, Mason PA.** Predicted SAR in Sprague-Dawley rat as a function of permittivity values. *Bioelectromagnetics* 22: 384–400, 2001.
31. **Garcin JM, Bronstein JA, Cremades S, Courbin P, Cointet F.** Acute liver failure is frequent during heat stroke. *World J Gastroenterol* 14: 158–159, 2008.
32. **Giacchino JL, Horowitz JM, Horwitz BA.** Simulation of the thermoregulatory system of rats exposed concurrently to cold and to acceleration fields. *Comput Biol Med* 9: 205–211, 1979.
33. **Gordon CJ.** *Temperature Regulation in Laboratory Rodents*. Cambridge, UK: Cambridge University Press, 1993, p. 16–17.
34. **Gordon CJ, Puckett E, Padnos B.** Rat tail skin temperature monitored noninvasively by radiotelemetry: characterization by examination of vasomotor responses to thermomodulatory agents. *J Pharmacol Toxicol Methods* 47: 107–114, 2002.
35. **Gordon RG, Roemer RB, Horvath SM.** A mathematical model of the human temperature regulatory system–transient cold exposure response. *IEEE Trans Biomed Eng* 23: 434–444, 1976.
36. **Greenberg JA.** Organ metabolic rates and aging: two hypotheses. *Med Hypotheses* 52: 15–22, 1999.
37. **Gribok AV, Buller MJ, Hoyt RW, Reifman J.** A real-time algorithm for predicting core temperature in humans. *IEEE Trans Inf Technol Biomed* 14: 1039–1045, 2010.
38. **Gribok AV, Buller MJ, Reifman J.** Individualized short-term core temperature prediction in humans using biomathematical models. *IEEE Trans Biomed Eng* 55: 1477–1487, 2008.
39. **Grogan H, Hopkins PM.** Heat stroke: implications for critical care and anaesthesia. *Br J Anaesth* 88: 700–707, 2002.
40. **Grosman B, Shaik OS, Helwig BG, Leon LR, Doyle FJ 3rd.** A physiological systems approach to modeling and resetting of mouse thermoregulation under heat stress. *J Appl Physiol* 111: 938–945, 2011.
41. **Gwosdow AR, Besch EL.** Effect of thermal history on the rat's response to varying environmental temperature. *J Appl Physiol* 59: 413–419, 1985.
42. **Hagiwara S, Iwasaka H, Shingu C, Matsumoto S, Uchida T, Noguchi T.** High-dose antithrombin III prevents heat stroke by attenuating systemic inflammation in rats. *Inflamm Res* 59: 511–518, 2010.
43. **Haly AR, Snaith JW.** Calorimetry of rat tail tendon collagen before and after denaturation—heat of fusion of its absorbed water. *Biopolymers* 10: 1681–1699, 1971.
44. **Hirata A, Masuda H, Kanai Y, Asai R, Fujiwara O, Arima T, Kawai H, Watanabe S, Lagroye I, Veyret B.** Computational modeling of temperature elevation and thermoregulatory response in the brains of anesthetized rats locally exposed at 1.5 GHz. *Phys Med Biol* 56: 7639–7657, 2011.
45. **Hoque M, Gandhi OP.** Temperature distributions in the human leg for VLF-VHF exposures at the ANSI-recommended safety levels. *IEEE Trans Biomed Eng* 35: 442–449, 1988.
46. **Horowitz JM, Erskine LK.** Central regulation of temperature in cold environments. 1. A dynamic model with two temperature inputs. *Comput Biomed Res* 6: 57–73, 1973.
47. **Hsiao SH, Chang CP, Chiu TH, Lin MT.** Resuscitation from experimental heatstroke by brain cooling therapy. *Resuscitation* 73: 437–445, 2007.
48. **Incropera FP, DeWitt DP, Bergman TL, Lavine AS.** *Fundamentals of Heat and Mass Transfer* (6th ed.). Hoboken, NJ: Wiley, 2006, p. 423–428.
49. **Keenan MA, Stabin MG, Segars WP, Fernald MJ.** RADAR realistic animal model series for dose assessment. *J Nucl Med* 51: 471–476, 2010.
50. **Kleiber M.** Body size and metabolism. *Hilgardia* 6: 315–353, 1932.
51. **Kregel KC, Wall PT, Gisolfi CV.** Peripheral vascular responses to hyperthermia in the rat. *J Appl Physiol* 64: 2582–2588, 1988.
52. **Lees S, Tao NJ, Lindsay SM.** Studies of compact hard tissues and collagen by means of Brillouin light scattering. *Connect Tissue Res* 24: 187–205, 1990.
53. **Leon LR, Blaha MD, DuBose DA.** Time course of cytokine, corticosterone, and tissue injury responses in mice during heat strain recovery. *J Appl Physiol* 100: 1400–1409, 2006.
54. **Leon LR, Gordon CJ, Helwig BG, Rufolo DM, Blaha MD.** Thermoregulatory, behavioral, and metabolic responses to heatstroke in a conscious mouse model. *Am J Physiol Regul Integr Comp Physiol* 299: R241–R248, 2010.
55. **Leon LR, Helwig BG.** Heat stroke: role of the systemic inflammatory response. *J Appl Physiol* 109: 1980–1988, 2010.
56. **Liu Z, Li B, Tong H, Tang Y, Xu Q, Guo J, Su L.** Pathological changes in the lung and brain of mice during heat stress and cooling treatment. *World J Emerg Med* 2: 50–53, 2011.
57. **Marqa MF, Colin P, Nevoux P, Mordon SR, Betrouni N.** Focal laser ablation of prostate cancer: numerical simulation of temperature and damage distribution. *Biomed Eng Online* 10: 45, 2011.
58. **Mason PA, Walters TJ, Fanton JW, Erwin DN, Gao JH, Roby JW, Kane JL, Lott KA, Lott LE, Blystone RV.** Database created from magnetic resonance images of a Sprague-Dawley rat, rhesus monkey, and pigmy goat. *FASEB J* 9: 434–440, 1995.
59. **Murakami DM, Horwitz BA, Fuller CA.** Circadian rhythms of temperature and activity in obese and lean Zucker rats. *Am J Physiol Regul Integr Comp Physiol* 269: R1038–R1043, 1995.
60. **Nelson DA.** Invited editorial on "Pennes' 1948 paper revisited". *J Appl Physiol* 85: 2–3, 1998.
61. **Nelson NG, Collins CL, Comstock D, McKenzie LB.** Exertional heat-related injuries treated in Emergency Departments in the U.S., 1997–2006. *Am J Prev Med* 40: 54–60, 2011.
62. **Oliver RE, Jones AF, Rowland M.** A whole-body physiologically based pharmacokinetic model incorporating dispersion concepts: short and long time characteristics. *J Pharmacokinet Pharmacodyn* 28: 27–55, 2001.
63. **Peng B, Andrews J, Nestorov I, Brennan B, Nicklin P, Rowland M.** Tissue distribution and physiologically based pharmacokinetics of antisense phosphorothioate oligonucleotide ISIS 1082 in rat. *Antisense Nucleic A* 11: 15–27, 2001.
64. **Pennes HH.** Analysis of tissue and arterial blood temperatures in the resting human forearm. *J Appl Physiol* 1: 93–122, 1948.
65. **Pisacane VL, Kuznetz LH, Logan JS, Clark JB, Wissler EH.** Thermoregulatory models of space shuttle and space station activities. *Aviat Space Environ Med* 78: A48–A55, 2007.
66. **Quesson B, de Zwart JA, Moonen CT.** Magnetic resonance temperature imaging for guidance of thermotherapy. *J Magn Reson Imaging* 12: 525–533, 2000.
67. **Raman ER, Vanhuyse VJ, Roberts MF.** Mathematical circulation model for the blood-flow-heat-loss relationship in the rat tail. *Phys Med Biol* 32: 859–875, 1987.
68. **Refinetti R.** Metabolic heat production, heat loss and the circadian rhythm of body temperature in the rat. *Exp Physiol* 88: 423–429, 2003.
69. **Ruis JF, Rietveld WJ, Buys JP.** Properties of parametric photic entrainment of circadian rhythms in the rat. *Physiol Behav* 50: 1233–1239, 1991.
70. **Sakurada S, Shido O, Fujikake K, Nagasaka T.** Relationship between body core and peripheral temperatures at the onset of thermoregulatory responses in rats. *Jpn J Physiol* 43: 659–667, 1993.
71. **Samaras T, Regli P, Kuster N.** Electromagnetic and heat transfer computations for non-ionizing radiation dosimetry. *Phys Med Biol* 45: 2233–2246, 2000.
72. **Sato S, Hatanaka T, Ohshima K, Endoh M, Katayama K, Kakemi M, Koizumi T.** Effect of environmental temperature on thermal response to chlorpromazine. I. Simulation of temperature regulation in rats. *J Pharmacobiodyn* 9: 997–1001, 1986.
73. **Shido O, Sakurada S, Kohda W, Nagasaka T.** Day-night changes of body temperature and feeding activity in heat-acclimated rats. *Physiol Behav* 55: 935–939, 1994.
74. **Stricker EM, Hainsworth FR.** Evaporative cooling in the rat: interaction with heat loss from the tail. *Q J Exp Physiol Cogn Med Sci* 56: 231–241, 1971.
75. **Trakic A, Crozier S, Liu F.** Numerical modelling of thermal effects in rats due to high-field magnetic resonance imaging (0.5–1 GHz). *Phys Med Biol* 49: 5547–5558, 2004.

76. **Trakic A, Liu F, Crozier S.** Transient temperature rise in a mouse due to low-frequency regional hyperthermia. *Phys Med Biol* 51: 1673–1691, 2006.
77. **Usui S, Takahashi Y, Okazaki T.** Range of entrainment of rat circadian rhythms to sinusoidal light-intensity cycles. *Am J Physiol Regul Integr Comp Physiol* 278: R1148–R1156, 2000.
78. **Vanhoutte G, Verhoye M, Raman E, Roberts M, Van der Linden A.** In-vivo non-invasive study of the thermoregulatory function of the blood vessels in the rat tail using magnetic resonance angiography. *NMR Biomed* 15: 263–269, 2002.
79. **Wallace RF, Kriebel D, Punnett L, Wegman DH, Amoroso PJ.** Prior heat illness hospitalization and risk of early death. *Environ Res* 104: 290–295, 2007.
80. **Wang H, Ma S.** The cytokine storm and factors determining the sequence and severity of organ dysfunction in multiple organ dysfunction syndrome. *Am J Emerg Med* 26: 711–715, 2008.
81. **Wang Z, O'Connor TP, Heshka S, Heymsfield SB.** The reconstruction of Kleiber's law at the organ-tissue level. *J Nutr* 131: 2967–2970, 2001.
82. **Wauschkuhn CA, Witte K, Gorbey S, Lemmer B, Schilling L.** Circadian periodicity of cerebral blood flow revealed by laser-Doppler flowmetry in awake rats: relation to blood pressure and activity. *Am J Physiol Heart Circ Physiol* 289: H1662–H1668, 2005.
83. **Weigand K, Riediger C, Stremmel W, Flechtenmacher C, Encke J.** Are heat stroke and physical exhaustion underestimated causes of acute hepatic failure? *World J Gastroenterol* 13: 306–309, 2007.
84. **Werner J, Buse M.** Temperature profiles with respect to inhomogeneity and geometry of the human body. *J Appl Physiol* 65: 1110–1118, 1988.
85. **Wissler EH.** Pennes' 1948 paper revisited. *J Appl Physiol* 85: 35–41, 1998.
86. **Wu L, Zhang G, Luo Q, Liu Q.** An image-based rat model for Monte Carlo organ dose calculations. *Med Phys* 35: 3759–3764, 2008.
87. **Wu Y, Jiji LM, Lemons DE, Weinbaum S.** A non-uniform three-dimensional perfusion model of rat tail heat transfer. *Phys Med Biol* 40: 789–806, 1995.
88. **Yang HH, Chang CP, Cheng RT, Lin MT.** Attenuation of acute lung inflammation and injury by whole body cooling in a rat heatstroke model. *J Biomed Biotechnol* 2009: 768086, 2009.
89. **Zeller L, Novack V, Barski L, Jotkowitz A, Almog Y.** Exertional heatstroke: clinical characteristics, diagnostic and therapeutic considerations. *Eur J Intern Med* 22: 296–299, 2011.
90. **Zhu L, Diao C.** Theoretical simulation of temperature distribution in the brain during mild hypothermia treatment for brain injury. *Med Biol Eng Comput* 39: 681–687, 2001.